Original scientific paper
https://doi.org/10.33180/InfMIDEM2024.302

Informacije MIDEM
Journal of Microelectronics, Electronic Components and Materials
Vol. 54, No. 3(2024), XX – XX

Aerosol-Deposition-Derived Graphite Thick Films for Electrochemical Sensors

Matej Šadl[1,+], Barbara Repič[1,2,+], Ivana Goričan[1,2], Danjela Kuščer[1,2] and Hana Uršič[1,2]

[1]Electronic Ceramics Department, Jožef Stefan Institute, Ljubljana, Slovenia
[2]Jožef Stefan International Postgraduate School, Ljubljana, Slovenia
[+]M.Š. and B.R. contributed equally

Abstract: Disposable electrochemical (EC) sensors are usually manufactured by screen printing and post-deposition temperature curing of the sensor's components. However, complete removal of an organic vehicle requires curing at temperatures of a few hundred °C, which can lead to electrode-substrate incompatibilities and limit the choice of material. In this work, graphite thick-film electrodes without additives were deposited on polyimide substrates at room temperature using the aerosol-deposition method. The resulting thick films had good adhesion, a defect-free surface, a thickness of a few micrometers, a root-mean-square roughness of 0.68 µm and sheet resistance of 27 Ω/sq. Scanning electron microscopy of the film surface revealed good particle compaction, while the X-ray diffraction analysis showed no peak broadening of the graphite thick films, which indicates a different deposition mechanism than that normally observed for ceramic powders. The EC properties of the graphite working electrodes were evaluated using cyclic voltammetry. The graphite films showed a low capacitive current of 0.114 mA, good reversibility of the redox process, a high EC active surface area of 1.44 cm^2/cm_{geo}^2 and a standard heterogeneous electron-transfer-rate constant of 0.0019 $cm \cdot s^{-1}$. The aerosol-deposited graphite thick-film electrodes show potential for the EC detection of a broad range of chemicals.

Keywords: graphite electrode; electrochemical detection; aerosol deposition; room-temperature process; polyimide foil

Debele plasti grafita nanešene v aerosolu za elektrokemijske senzorje

Izvleček: Elektrokemijski (EK) senzorji za enkratno uporabo se običajno izdelujejo tako, da komponente senzorja natisnemo s sitotiskom ter jih nato temperaturno obdelamo. Za popolno odstranitev organskega nosilca je plasti potrebno segreti do nekaj sto °C, kar lahko privede do nezdružljivosti med elektrodo in podlago ter omeji izbiro materiala. V tej raziskavi smo z metodo nanosa plasti v aerosolu pri sobni temperaturi pripravili debeloplastne grafitne elektrode brez dodatkov na poliimidne podlage. Tako pripravljene debele plasti se dobro držijo podlage, imajo površino brez vidnih defektov, debelino nekaj mikrometrov, hrapavost 0.68 µm in plastno upornost 27 Ω/sq. Z vrstično elektronsko mikroskopijo smo na površini plasti opazili kompaktno strukturo delcev. Pri rentgenski difrakciji debelih plasti grafita ne zaznamo širitve vrhov, kar nakazuje, da je mehanizem nanašanja pri grafitu drugačen kot je običajno za keramični prah. EK lastnosti grafitnih delovnih elektrod smo analizirali s ciklično voltametrijo. Grafitne plasti izkazujejo nizek kapacitivni tok z vrednostjo 0.114 mA, dobro reverzibilnost redoks procesa, veliko EK aktivno površino z vrednostjo 1.44 cm^2/cm_{geo}^2 in visok standardni koeficient heterogene reakcije z vrednostjo 0.0019 $cm \cdot s^{-1}$. Debeloplastne grafitne elektrode pripravljene z metodo nanosa plasti v aerosolu so primerne za EK detekcijo številnih kemikalij.

Ključne besede: grafitna elektroda; elektrokemijska detekcija; metoda nanašanja plasti v aerosolu; priprava pri sobni temperaturi; poliimidna folija

* *Corresponding Authors' e-mail: hana.ursic@ijs.si, danjela.kuscer@ijs.si*

1 Introduction

The amount of research on electrochemical (EC) sensors is increasing owing to the requirement for the point-of-care and on-site detection of various compounds such as pharmaceuticals, pesticides, toxins and heavy metals [1]–[8]. These are widely utilized in agriculture and the food industries as well as in environmental and biomedical applications. The applications for disposable EC sensors dictate many requirements: good selectivity and sensitivity for a broad range of EC active species, reproducibility of the results, miniature and portable systems, ease of use and cost-effective production with easy scale-up possibilities [8]–[11].

The EC sensors consist of three electrodes, i.e., the counter, reference and working electrode (WE). In disposable EC sensors the electrodes are integrated on selected substrates, commonly by screen printing and the subsequent firing of the deposited layers at elevated temperatures. The WE is a key component and should have high electrical conductivity and a high specific surface area.

Screen printing is the most commonly used method for depositing films that are typically a few tens of µm thick. It is a mature, commercially available technology, which offers patterning of the structures with good reproducibility on laboratory and industrial scales [11]–[14].

Although the screen-printing method is widely adopted, there are some challenges that need to be considered. In printing techniques, the ink or paste consists of a solid material dispersed in an organic vehicle. To obtain good functional properties of the thick film, the organic vehicle must be removed during the processing. To remove the organic vehicle and to densify the thick film, a temperature of a few hundred °C is needed [14], [15]. Due to the degradation of carbon in air, annealing at higher temperatures requires an inert atmosphere [16]. However, high-temperature curing can lead to electrode-substrate incompatibilities, which significantly limit the choice of substrate materials. To avoid this shortcoming, the EC active materials should be deposited at low temperature and without additives.

The aerosol deposition (AD) method, sometimes known as powder aerosol deposition, enables the direct deposition of functional materials in the form of micrometre-sized dry powders without the use of additives [17]. The deposition mechanism is based on the impact of the particles, and the film's consolidation occurs at room temperature, due to the high kinetic energy of the sprayed particles [18]–[21]. AD is a room-temperature process that enables the integration of functional materials on low-melting point and flexible substrates [22]–[25]. As a result, AD offers good material compatibility. It is generally used for the deposition of ceramic films, but metals can also be deposited. However, research on metal deposition is still in its beginnings. So far, the following materials have been deposited using AD: Cu [26], [27], Ag [28], [29], Al [30], [31], Fe [32] Fe-based amorphous alloys [33], $(Bi,Sb)_2Te_3$ [34], [35], rare-earth magnets [36], [37] and graphite [38].

Carbon-based materials are commonly used as the WE in EC sensors. They are non-toxic, low-cost, have high electrical conductivity and allow the detection of various compounds such as pharmaceuticals, pesticides, toxins and heavy metals [39]–[43].

In this study we processed a-few-µm-thick graphite films on a polyimide substrate by AD at room temperature and without any post-deposition curing. The graphite thick films were structurally and microstructurally characterized using contact profilometry, X-ray diffraction, atomic force microscopy and scanning electron microscopy. Their EC properties were investigated by cyclic voltammetry. The purpose was to study the properties of graphite thick films prepared by a relatively new AD method and to assess the suitability of the aerosol-deposited thick films for use in EC applications.

2 Materials and Methods

A commercially available graphite powder (graphite flake, 99.8 %, 043209, Alfa Aesar) was sieved through a mesh (with 80-µm openings) and vacuum dried at 80 °C, before being aerosol deposited (AD) onto the substrate. A commercially available polyimide (PI) foil (Kapton HN, DuPont, DE, USA) with a thickness of 125 µm was used as a substrate. The AD equipment was provided by InVerTech, Germany. A schematic of the AD setup is shown in [44]. During the AD the process parameters (Table 1) were kept constant. After the film's deposition the thick-film samples were cleaned by gently blowing them with air.

Table 1: Process parameters used during the AD.

Process parameter	Value
Pressure in the deposition chamber	90 mbar
Pressure in aerosol chamber	0.6 mbar
Nozzle geometry (slit size)	$(0.5 \cdot 10)$ mm^2
Carrier gas species	N_2
Gas flow rate	1 L·min^{-1}
Distance between nozzle and substrate	5 mm
Sweep speed	5 mm·s^{-1}

The particle size distribution of the initial graphite powder was determined in isopropanol using a light-scattering laser granulometer (S3500, Microtrac, PA, USA).

The X-ray diffraction (XRD) analysis was performed with a benchtop X-ray diffractometer (MiniFlex 600-C, Rigaku, Japan) using Cu-K_α radiation. Diffraction patterns were recorded in the Bragg–Brentano geometry using a silicon strip detector (D/teX Ultra) in a 2θ range of 10°–60° with a step of 0.01° and 0.06 s/step. The software X'Pert HighScore Plus 3.0e (PANalytical, Almelo, The Netherlands) was used to analyse the XRD patterns and strip the Cu-$K_{\alpha 2}$ component.

The microstructures of the graphite powder and the surface of th graphite thick films were analysed using a field-emission scanning electron microscope (FE-SEM, JSM 7600F, Jeol, Japan), equipped with

secondary electron and backscattered electron detectors. Before the analysis, the graphite powder was spread on the carbon tape.

The topography of the graphite thick films was analysed using contact stylus profilometry (DektakXT, Bruker, MA, USA) and atomic force microscopy (AFM, MFP-3D, Asylum Research, CA, USA). The thickness and root-mean-square surface roughness (R_q) of the thick films were evaluated from a line profile measured with a contact profilometer using the software Vision64 (Bruker, MA, USA). The thickness was evaluated from the step height of the film after curvature removal using a quadratic polynomial. R_q was evaluated from the 2-mm roughness profile (length of 2 mm) obtained after filtering the total profile using Gaussian regression (cut off 0.8 mm). In the AFM analysis a Si tip on a Si/Al cantilever with a diameter of ~7 nm (AC240TSR3, Asylum Research, CA, USA) was used for scanning in AC topography mode. The root-mean-square surface roughness R_q^{AFM} was also evaluated from the AFM map scans (with dimensions 80 µm x 80 µm).

The sheet resistance (R_s) of the thick films was measured using the four-point probe technique, with the probes arranged equidistantly in a line. The R_s of the thick film was calculated from the measured voltage drop between the two inner probes and the current. A correction factor of 0.795 was used [45].

EC experiments were performed using a potentiostat-galvanostat (Multi Autolab M 204, Methrom, The Netherlands) controlled by Nova 2.1.5 software. A conventional three-electrode cell configuration was used. The graphite thick films processed by AD were used as the WE, together with a conventional Ag/AgCl reference electrode and a platinum-sheet counter electrode (both from Methrom). The measurements were carried out in deaerated solutions at 25 °C. Cyclic voltammograms were measured between –0.2 V and 0.6 V at a constant scan rate (ν) of 20, 50, 100, 200 and 500 mV·s^{-1}. The measurements were performed in a 0.1-M phosphate buffer solution (PBS) used as an electrolyte and in a 0.005-M equimolar solution of $Fe(CN)_6^{3-/4-}$ (HCF) as a redox probe dissolved in the PBS. The voltammograms measured at 100 mV·s^{-1} were characterized to determine the capacitive current (i_{cap}) in the PBS, the peak-to-peak separation (ΔE_{pp}) and the cathodic-to-anodic peak current ratio (i_{pc}/i_{pa}) in HCF. From the measurements at different scan rates, the electrochemically active surface area was determined from the slope of the linear dependence of the peak current as a function of the square root of the scan rate using the Randles-Ševćik equation. It was normalised using the geometric surface area to obtain a real electrochemically active surface area (A_{ecsa}) [9]. Cyclic voltammograms recorded at different scan rates were also used to determine a standard heterogeneous electron-transfer-rate constant (k^0) using the Nicholson method [46], in which the k^0 of a quasi-reversible reaction is related to a dimensionless kinetic parameter (Ψ), calculated as a function of ΔE_{pp} at different scan rates. The electrodes were also used to determine operating potential window (OPW), which was assessed based on the qualitative inspection of a series of cyclic voltammograms, obtained by incrementally increasing or decreasing the vertex potential of the sweep range in 0.05-V increments. The limits of the OPW are identified as the potential at which the current intensity was in the same range as the peak current of the redox probe.

The mechanical stability of the graphite thick films was additionally tested by immersing and rinsing them in organic solvents, i.e., methanol, ethanol and acetone.

3 Results

The graphite powder, which resulted in few-micrometer-thick films, was analysed using laser granulometry and SEM. The volumetric particle size distribution of the graphite powder measured by laser granulometry is shown in Figure 1(a). The distribution is monomodal with the particle size ranging between 1.6 µm and 148 µm. The median (d_{50}) particle size is 16.6 µm, represented by an orange vertical line. For the successful AD of ceramics, the typically reported particle size is between 0.2 µm and 2 µm [18]. Also for the AD of metals, the particle size window for a successful deposition is between 1 µm and 10 µm [30], [47]. However, in our case the AD of graphite powder was successful using much larger particles than typically used in AD. In the literature, there are not many reports that show a successful AD using particles with d_{50} larger than 10 µm. These cases are limited to Nd-Fe-B magnets [37], MAX phase materials [48] and glass [49].

The SEM micrographs, taken with a secondary-electron detector in Figure 1(b, c), reveal the morphology of the graphite powder. Figure 1(b) shows large, agglomerated particles with round-shaped surfaces. The agglomerates exceed 40 µm in diameter (red dashed circle). The agglomeration is in agreement with the laser granulometry data (Figure 1(a)). On the other hand, Figure 1(c) shows particles that have an irregular shape, including plate-like surfaces that indicate the easy cleavage of the graphite flake-type particles. The smallest particles are of the order of 1 µm.

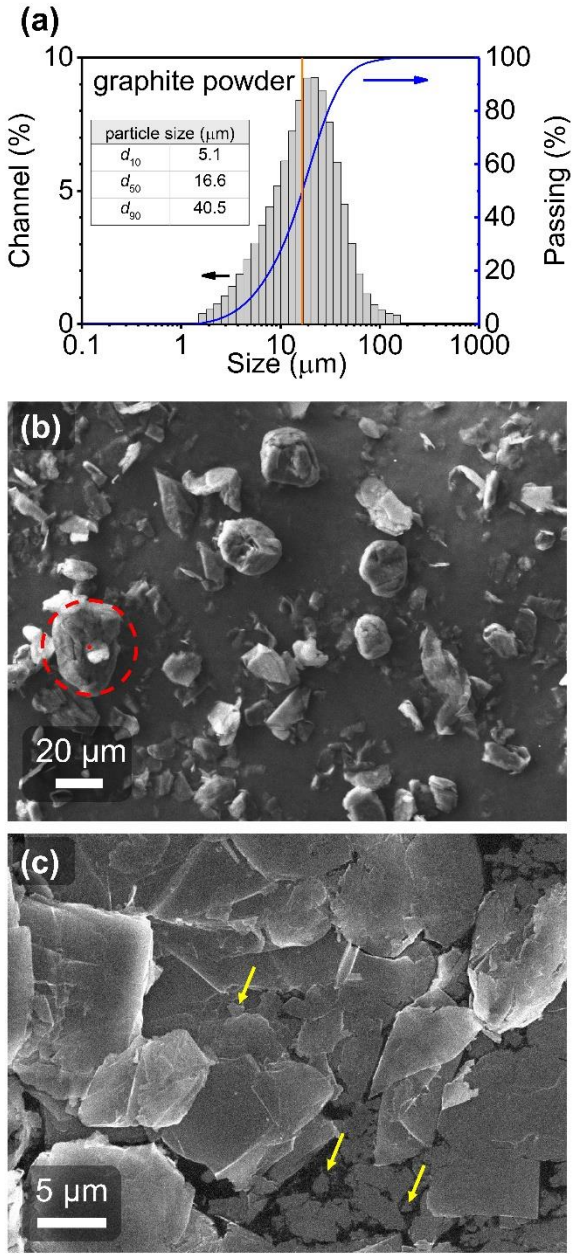

Figure 1: Analysis of the graphite powder. (a) Volumetric particle size distribution (grey) and cumulative curves (blue) evaluated from the laser granulometry. The vertical orange line represents the median (d_{50}) particle size. The d_{10}, d_{50} and d_{90} are also displayed in the inset table. (b, c) SEM images taken with a secondary-electron detector. The red dashed circle with diameter of 40 µm marks a large agglomerate, while the smallest particles, around 1 µm, are marked with yellow arrows.

The AD of the graphite powder on a PI substrate was successful, resulting in good adhesion of the film to the substrate and defect-free appearance of the film's surface, as seen in Figure 2(a). A line scan across the deposited film is shown in Figure 2(b) and reveals an even film thickness of 4.4 µm. The root-mean-square roughness (R_q) reaches 0.68 µm, which is at least 3-times higher than reported for Al_2O_3 films and ceramic-metal (Al_2O_3-Al) multilayered thick films prepared by AD [18], [30]. A high surface roughness indicates a high specific surface area, which is advantageous in EC sensing applications. Note that after the AD the graphite film is still susceptible to abrasion. The sheet resistance (R_S) of 27 Ω/sq confirmed sufficient conductivity of the film for the EC measurement. The resistance is comparable to that of screen-printed conductive carbon films [50].

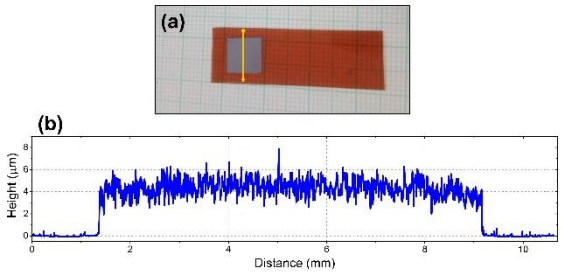

Figure 2: (a) Photograph of the deposited graphite thick film on a PI substrate. The orange line represents the position of the line scan. (b) Line profile measured by contact profilometry.

The XRD patterns of the graphite powder and deposited thick films are shown in Figure 3. Both powder and film contain a graphite phase (PDF 075-2078) [51], with the most prominent reflection (002) at 2θ of 26.5°. Note that the powder also contains a trace amount of some other graphite phase, which overlaps with the (002) reflection. After the deposition, the peak position of the graphite phase does not change and the peak width does not increase. This shows that there is no crystallite size reduction and build-up of microstrain due to the impacting particles, which is typically observed in the deposition of ceramic thick films [23], [52]. The XRD pattern of the graphite film also contains additional peaks and an increased background level arising from the PI substrate.

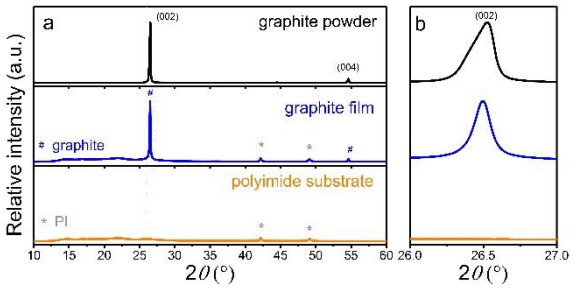

Figure 3: XRD patterns of the graphite powder (black), graphite thick film (blue) and blank PI substrate (orange). (a) XRD patterns in 2θ range 10°–60°, (b) close-up view of the region of the most intense graphite peak.

The surface topography of the graphite thick films was analysed using AFM (Figure 4) and SEM (Figure 5). Figure 4(a, b, c) shows the AFM height, deflection and tapping amplitude modes, respectively. The height image (Figure 4(a)) shows obvious craters, which contribute to the high R_q^{AFM}, reaching 0.48 µm. Both the AFM and SEM images reveal irregularly shaped particles. An interesting observation is the straight features (yellow arrows in Figure 4 and Figure 5(b)) that resemble sharp-edged particles, which indicates the flake-like nature of the deposited graphite film. From the SEM surface view, good particle compaction can be observed. In particular, the SEM image taken with a backscattered-electron detector (Figure 5(b)) reveals no clear pores or voids between the deposited particles. The backscattered-electron detector is very appropriate for evaluating the film's homogeneity as it gives a high contrast between the compact and porous regions.

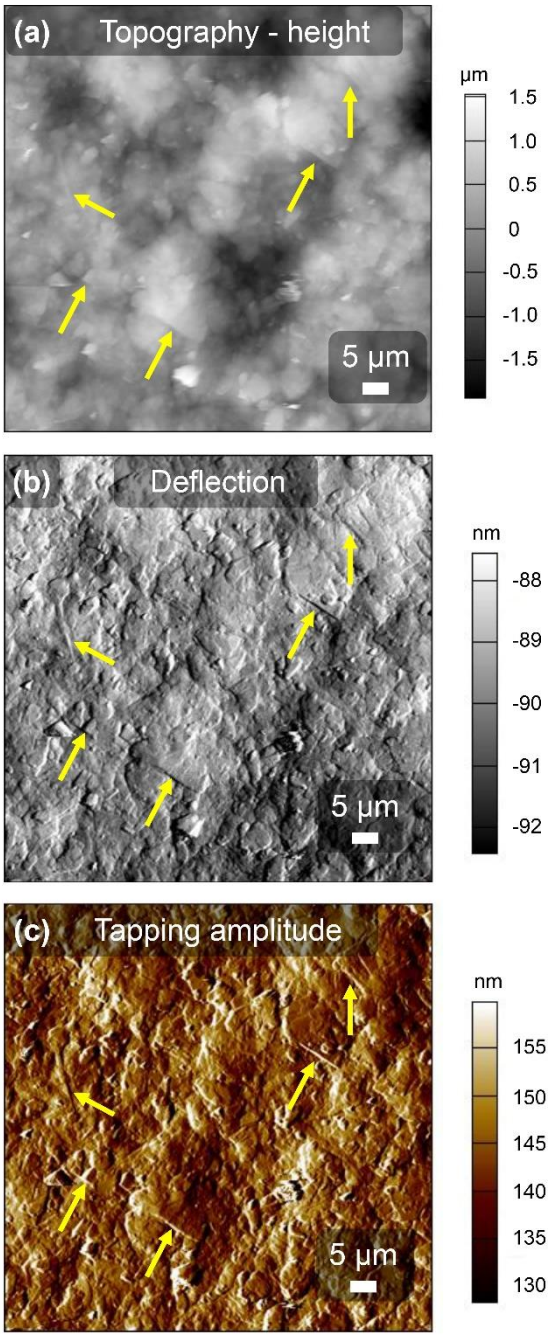

Figure 4: AFM map scans of the surface of graphite thick films. (a) height, (b) deflection, and (c) tapping amplitude. Yellow arrows designate sharp edges of the flake-like particles.

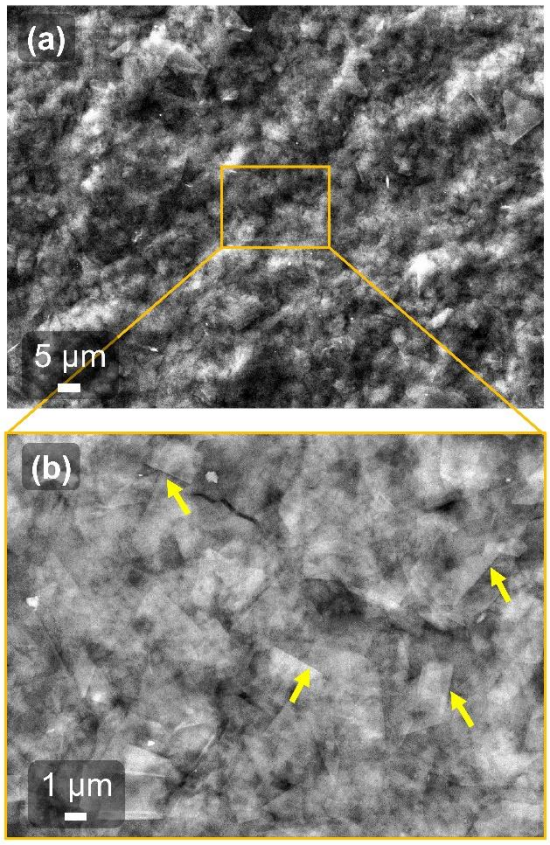

Figure 5: The SEM images of the graphite thick film in surface view. The micrographs in (a) and (b) were taken with secondary-electron and backscattered-electron detector, respectively. Yellow arrows designate sharp edges of flake-like particles.

An EC analysis of the graphite thick-film WE was made by cyclic voltammetry (Figure 6). The voltammogram measured in the PBS shows a low background with an i_{cap} of 0.114 mA, determined as the difference between cathodic and anodic currents at 0.2 V. For the characterization of the voltammogram recorded in HCF, we determined the anodic (i_{pa}) and cathodic peak currents (i_{pc}), which were corrected with capacitive currents measured in the PBS at the same potentials. The currents observed in both the PBS and HCF are higher than those observed for commercially available, screen-printed electrodes [9], or screen-printed graphite-based WEs [53], [54]. From the i_{pc}/i_{pa} ratio of 0.99, we can confirm the good reversibility of the redox process. From the anodic (E_{pa}) and cathodic peak potentials (E_{pc}), we determined an ΔE_{pp} of 176 mV as the absolute difference between the two values, indicating that this redox couple exhibits a quasi-reversible behaviour at the graphite electrode prepared by AD [54].

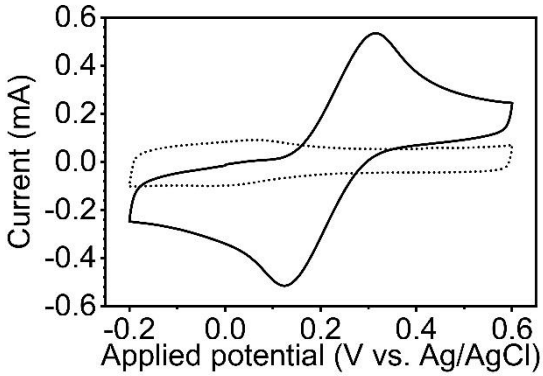

Figure 6: Cyclic voltammograms at 100 mV·s^{-1} of PBS (dotted line) and HCF (full line) at graphite thick-film WE.

The EC response of the WE at different scan rates is shown in Figure 7(a). According to the Randles-Ševčik equation, the peak current is proportional to A_{ecsa}, which can in turn be calculated from the slope of the linear relationship between i_{pc} or i_{pa} and square root of the scan rate, shown in Figure 7(b). The data shows good linearity for both peak currents, but slightly different slopes. A_{ecsa} was calculated for both peaks, and their average value was 1.44 ± 0.06 cm^2/cm$_{geo}^2$. This value is higher than the screen-printed graphite electrode (0.79 cm^2/cm$_{geo}^2$) [54]. The increase in A_{ecsa} could be attributed to the high surface roughness of the graphite thick films prepared by AD.

Since the ΔE_{pp} of the quasi-reversible process changes with the scan rate, we used cyclic voltammograms measured at different scan rates to plot how a dimensionless kinetic parameter Ψ varies with the inverse square root of the scan rate, as shown in Figure 7(c). A k^0 of 1.9·10^{-3} cm·s^{-1} was then calculated from the slope by the Nicholson method at ν = 20–500 mV·s^{-1} (ΔE_{pp} = 122–354 mV). Although the ΔE_{pp} at the highest scan rate used exceeds the range for which the Nicholson method is valid, all points show good linearity. Compared to values reported by Trachioti et al. [54] for graphite screen-printed electrodes, we obtained similar k^0 values. To determine in which potential range the electrode has a stable response, we also determined its OPW, which is from –0.9 V to 1.2 V. Electrode stability in the anodic direction makes it very suitable for the detection of phenolic compounds such as bisphenol A [6], dihydroxybenzene isomers such as hydroquinone, catechol and resorcinol [7], parabens [55], quinolone antibiotics [56], organohalides [57], as well as 4-nitrophenol and dopamine [58]. The graphite thick films were also mechanically stable and did not degrade or delaminate from the substrate when immersed in and rinsed with methanol, ethanol or acetone. Therefore, the films can also be used for the detection of analytes that require non-aqueous electrolytes. We can conclude that AD graphite thick films are applicable as

working electrodes in EC sensors for the detection of various organic compounds.

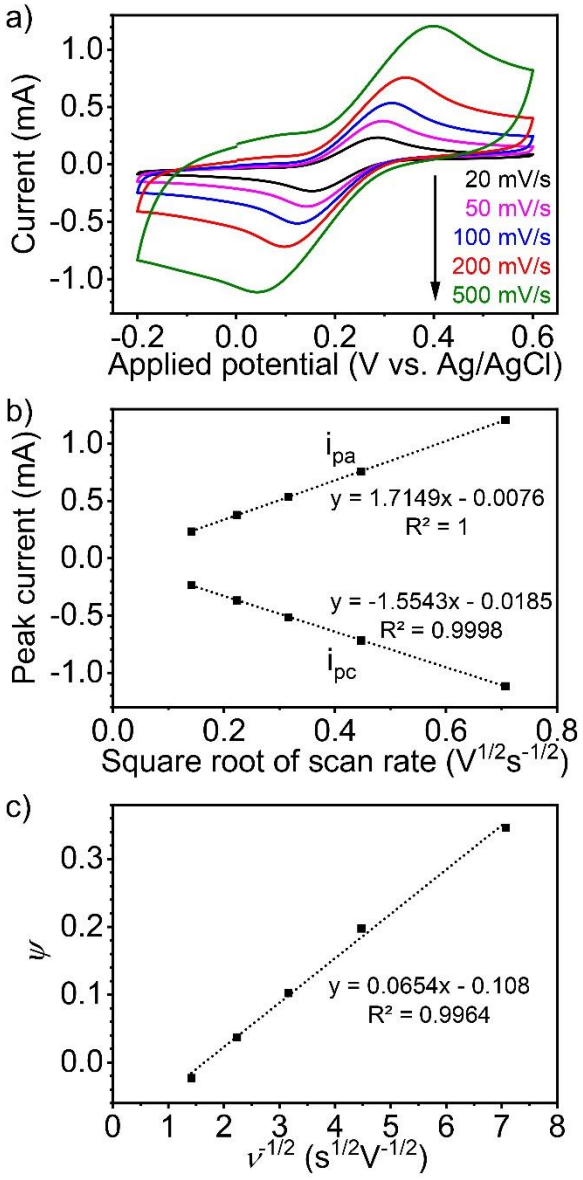

Figure 7: (a) Cyclic voltammograms of various scan rates of HCF for graphite thick-film WE, (b) plot of cathodic and anodic peak currents of HCF as a function of the square root of the scan rate, (c) plot of Ψ vs. $\nu^{1/2}$ for the reduction of HCF.

4 Conclusions

To avoid high temperatures in the fabrication of EC sensors, the AD method was used to process graphite thick films on PI substrates. The initial graphite powder consists of flake-type particles with an irregular shape that form large agglomerates. The powder particle size distribution shows a rather large d_{50} particle size of 16.6 µm, which is rarely reported for the AD method. However, AD was successful and resulted in ~4-µm-thick films with a defect-free appearance and an R_q of 0.68 µm. The SEM revealed good particle compaction of the film surface. The XRD patterns showed no reduction in the crystallite size and no increase in the microstrain after deposition. The graphite is therefore not subjected to the same deposition mechanism that is typical for ceramics. An EC analysis by cyclic voltammetry showed good reversibility of the redox process for graphite working electrodes with a large, real A_{ecsa} of 1.44 cm^2/cm_{geo}^2 and a k^0 of 0.0019 cm s^{-1}, comparable to those reported for graphite in the literature. A reasonable OPW between –0.9 V and 1.2 V also enables their use as working electrodes for the EC detection of a broad range of chemicals.

5 Acknowledgments

This work was funded by the Slovenian Research and Innovation Agency (research project N2-0212, J2–3049, and research core funding P2-0105), Ministry of Higher Education, Science and Innovation of Republic Slovenia (C3360-23-252004, M-ERA.NET) and the Jožef Stefan Institute Director's fund 2017-ULTRACOOL. The authors thank K. Spanou, N. Suban and V. Fišinger for assistance in the laboratory.

6 Conflict of Interest

The authors declare no conflict of interest. The founding sponsors had no role in the design of the study; in the collection, analyses, or interpretation of data; in the writing of the manuscript, and in the decision to publish the results.

7 References

[1] J. Baranwal, B. Barse, G. Gatto, G. Broncova, and A. Kumar, "Electrochemical Sensors and Their Applications: A Review," *Chemosensors*, vol. 10, no. 9, p. 363, 2022, https://doi.org/10.3390/chemosensors10090363.

[2] G. Maduraiveeran and W. Jin, "Nanomaterials based electrochemical sensor and biosensor platforms for environmental applications," *Trends Environ. Anal. Chem.*, vol. 13, pp. 10–23, 2017, https://doi.org/10.1016/j.teac.2017.02.001.

[3] K. Ashley, "Developments in electrochemical sensors for occupational and environmental health applications," *J. Hazard. Mater.*, vol. 102, no. 1, pp. 1–12, 2003, https://doi.org/10.1016/S0304-3894(03)00198-5.

[4] Y. Wang, H. Xu, J. Zhang, and G. Li,

"Electrochemical Sensors for Clinic Analysis," *Sensors*, vol. 8, no. 4, pp. 2043–2081, 2008, https://doi.org/10.3390/s8042043.

[5] Z. Shi, L. Xia, and G. Li, "Recent Progress of Electrochemical Sensors in Food Analysis," *Chemosensors*, vol. 11, no. 9, p. 478, 2023, https://doi.org/10.3390/chemosensors11090478.

[6] A. C. de Sá *et al.*, "Flexible Carbon Electrodes for Electrochemical Detection of Bisphenol-A, Hydroquinone and Catechol in Water Samples," *Chemosensors*, vol. 8, no. 4, p. 103, 2020, https://doi.org/10.3390/chemosensors8040103.

[7] M. M. I. Khan, M. A. Yousuf, P. Ahamed, M. Alauddin, and N. T. Tonu, "Electrochemical Detection of Dihydroxybenzene Isomers at a Pencil Graphite Based Electrode," *ACS Omega*, vol. 7, no. 33, pp. 29391–29405, 2022, https://doi.org/10.1021/acsomega.2c03651.

[8] J. P. Metters, R. O. Kadara, and C. E. Banks, "New directions in screen printed electroanalytical sensors: an overview of recent developments," *Analyst*, vol. 136, no. 6, p. 1067, 2011, https://doi.org/10.1039/c0an00894j.

[9] R. O. Kadara, N. Jenkinson, and C. E. Banks, "Characterisation of commercially available electrochemical sensing platforms," *Sensors Actuators, B Chem.*, vol. 138, no. 2, pp. 556–562, 2009, https://doi.org/10.1016/j.snb.2009.01.044.

[10] R. Umapathi, S. M. Ghoreishian, S. Sonwal, G. M. Rani, and Y. S. Huh, "Portable electrochemical sensing methodologies for on-site detection of pesticide residues in fruits and vegetables," *Coord. Chem. Rev.*, vol. 453, p. 214305, 2022, https://doi.org/10.1016/j.ccr.2021.214305.

[11] C. E. Banks, C. W. Foster, and R. O. Kadara, *Screen-Printing Electrochemical Architectures*. Cham: Springer International Publishing, 2016.

[12] R. A. Dorey, *Ceramic Thick Films for MEMS and Microdevices*. Oxford: Elsevier, 2012.

[13] D. Kuscer, "Screen Printing," in *Encyclopedia of Materials: Technical Ceramics and Glasses*, vol. 1, Elsevier, 2021, pp. 227–232, https://doi.org/10.1016/B978-0-12-803581-8.12082-X.

[14] M. Kosec, D. Kuscer, and J. Holc, "Processing of Ferroelectric Ceramic Thick Films," in *Multifunctional Polycrystalline Ferroelectric Materials*, Dordrecht: Springer, 2011, https://doi.org/10.1007/978-90-481-2875-4_2.

[15] A. Mishra *et al.*, "Effect of annealing temperature on the performance of printable carbon electrodes for perovskite solar cells," *Org. Electron.*, vol. 65, pp. 375–380, 2019, https://doi.org/10.1016/j.orgel.2018.11.046.

[16] F. Cataldo, "A study on the thermal stability to 1000 °C of various carbon allotropes and carbonaceous matter both under nitrogen and in air," *Fullerenes, Nanotub. Carbon Nanostructures*, vol. 10, no. 4, pp. 293–311, 2002, https://doi.org/10.1081/FST-120016451.

[17] M. Schubert *et al.*, "Powder aerosol deposition method — novel applications in the field of sensing and energy technology," *Funct. Mater. Lett.*, vol. 12, no. 05, p. 1930005, 2019, https://doi.org/10.1142/s1793604719300056.

[18] D. Hanft, J. Exner, M. Schubert, T. Stöcker, P. Fuierer, and R. Moos, "An overview of the Aerosol Deposition method: Process fundamentals and new trends in materials applications," *J. Ceram. Sci. Technol.*, vol. 6, no. 3, pp. 147–181, 2015, https://doi.org/10.4416/JCST2015-00018.

[19] J. Akedo, "Room Temperature Impact Consolidation (RTIC) of Fine Ceramic Powder by Aerosol Deposition Method and Applications to Microdevices," *J. Therm. Spray Technol.*, vol. 17, no. 2, pp. 181–198, 2008, https://doi.org/10.1007/s11666-008-9163-7.

[20] M. Linz *et al.*, "Revealing the Deposition Mechanism of the Powder Aerosol Deposition Method Using Ceramic Oxide Core–Shell Particles," *Adv. Mater.*, p. 2308294, 2023, https://doi.org/10.1002/adma.202308294.

[21] R. Saunders, S. D. Johnson, D. Schwer, E. A. Patterson, H. Ryou, and E. P. Gorzkowski, "A Self-Consistent Scheme for Understanding Particle Impact and Adhesion in the Aerosol Deposition Process," *J. Therm. Spray Technol.*, vol. 30, no. 3, pp. 523–541, 2021, https://doi.org/10.1007/s11666-021-01164-4.

[22] N. H. Khansur, U. Eckstein, L. Benker, U. Deisinger, B. Merle, and K. G. Webber, "Room temperature deposition of functional ceramic films on low-cost metal substrate," *Ceram. Int.*, vol. 44, no. 14, pp. 16295–

16301, 2018, https://doi.org/10.1016/j.ceramint.2018.06.027.

[23] M. Sadl *et al.*, "Energy-storage-efficient $0.9Pb(Mg_{1/3}Nb_{2/3})O_3–0.1PbTiO_3$ thick films integrated directly onto stainless steel," *Acta Mater.*, vol. 221, p. 117403, 2021, https://doi.org/10.1016/j.actamat.2021.117403.

[24] M. Sadl, A. Lebar, J. Valentincic, and H. Ursic, "Flexible Energy-Storage Ceramic Thick-Film Structures with High Flexural Fatigue Endurance," *ACS Appl. Energy Mater.*, vol. 5, no. 6, pp. 6896–6902, 2022, https://doi.org/10.1021/acsaem.2c00518.

[25] M. Sadl *et al.*, "Multifunctional flexible ferroelectric thick-film structures with energy storage, piezoelectric and electrocaloric performance," *J. Mater. Chem. C*, vol. 11, no. 29, pp. 10058–10068, 2023, https://doi.org/10.1039/D3TC01555F.

[26] D. W. Lee, O. Y. Kwon, W. J. Cho, J. K. Song, and Y. N. Kim, "Characteristics and Mechanism of Cu Films Fabricated at Room Temperature by Aerosol Deposition," *Nanoscale Res. Lett.*, vol. 11, no. 1, 2016, https://doi.org/10.1186/s11671-016-1378-9.

[27] N. H. Khansur *et al.*, "Enhanced Electromechanical Response and Thermal Stability of $0.93(Na_{1/2}Bi_{1/2})TiO_3$-$0.07BaTiO_3$ Through Aerosol Deposition of Base Metal Electrodes," *Adv. Mater. Interfaces*, vol. 93, p. 2100309, 2021, https://doi.org/10.1002/admi.202100309.

[28] Y.-H. Kim, J.-W. Lee, H.-J. Kim, Y.-H. Yun, and S.-M. Nam, "Silver metallization for microwave device using aerosol deposition," *Ceram. Int.*, vol. 38, pp. S201–S204, 2012, https://doi.org/10.1016/J.CERAMINT.2011.04.083.

[29] M.-Y. Cho *et al.*, "Formation of silver films for advanced electrical properties by using aerosol deposition process," *Jpn. J. Appl. Phys.*, vol. 57, no. 11S, p. 11UF05, 2018, https://doi.org/10.7567/JJAP.57.11UF05.

[30] M. Sadl, U. Tomc, and H. Ursic, "Investigating the Feasibility of Preparing Metal–Ceramic Multi-Layered Composites Using Only the Aerosol-Deposition Technique," *Materials*, vol. 14, no. 16, p. 4548, 2021, https://doi.org/10.3390/ma14164548.

[31] V. Regis, M. Šadl, G. Brennecka, A. Bradeško, U. Tomc, and H. Uršič, "Investigation of Structural and Electrical Properties of Al_2O_3/Al Composites Prepared by Aerosol Co-Deposition," *Crystals*, vol. 13, no. 5, p. 850, 2023, https://doi.org/10.3390/cryst13050850.

[32] N. Leupold, S. Denneler, G. Rieger, and R. Moos, "Powder Treatment for Increased Thickness of Iron Coatings Produced by the Powder Aerosol Deposition Method and Formation of Iron–Alumina Multilayer Structures," *J. Therm. Spray Technol.*, vol. 30, no. 3, pp. 480–487, 2020, https://doi.org/10.1007/s11666-020-01098-3.

[33] J. Kwon, H. Park, I. Lee, and C. Lee, "Effect of gas flow rate on deposition behavior of Fe-based amorphous alloys in vacuum kinetic spray process," *Surf. Coatings Technol.*, vol. 259, pp. 585–593, 2014, https://doi.org/10.1016/j.surfcoat.2014.10.026.

[34] S. Baba, L. Huang, H. Sato, R. Funahashi, and J. Akedo, "Room-temperature fast deposition and characterization of nanocrystalline $Bi_{0.4}Sb_{1.6}Te_3$ thick films by aerosol deposition," *J. Phys. Conf. Ser.*, vol. 379, no. 1, p. 012011, 2012, https://doi.org/10.1088/1742-6596/379/1/012011.

[35] S. Baba, H. Sato, L. Huang, A. Uritani, R. Funahashi, and J. Akedo, "Formation and characterization of polyethylene terephthalate-based $(Bi_{0.15}Sb_{0.85})_2Te_3$ thermoelectric modules with $CoSb_3$ adhesion layer by aerosol deposition," *J. Alloys Compd.*, vol. 589, pp. 56–60, 2014, https://doi.org/10.1016/j.jallcom.2013.11.180.

[36] S. Sugimoto, T. Maeda, R. Kobayashi, J. Akedo, M. Lebedev, and K. Inomata, "Magnetic properties of Sm-Fe-N thick film magnets prepared by the aerosol deposition method," *IEEE Trans. Magn.*, vol. 39, no. 5, pp. 2986–2988, 2003, https://doi.org/10.1109/TMAG.2003.816715.

[37] S. Sugimoto *et al.*, "$Nd_2Fe_{14}B/Fe_3B$ nanocomposite film fabricated by aerosol deposition method," *J. Alloys Compd.*, vol. 408–412, pp. 1413–1416, 2006, https://doi.org/10.1016/j.jallcom.2005.04.044.

[38] C.-W. Ahn *et al.*, "Microstructure and electrochemical properties of graphite and C-coated $LiFePO_4$ films fabricated by aerosol deposition method for Li ion battery," *Carbon N. Y.*, vol. 82, pp. 135–142, 2015, https://doi.org/10.1016/j.carbon.2014.10.043.

[39] S. Michalkiewicz, A. Skorupa, and M.

Jakubczyk, “Carbon materials in electroanalysis of preservatives: A review,” *Materials*, vol. 14, no. 24, 2021, https://doi.org/10.3390/ma14247630.

[40] T. Gan and S. Hu, “Electrochemical sensors based on graphene materials,” *Microchim. Acta*, vol. 175, no. 1–2, pp. 1–19, 2011, https://doi.org/10.1007/s00604-011-0639-7.

[41] A. C. Power, B. Gorey, S. Chandra, and J. Chapman, “Carbon nanomaterials and their application to electrochemical sensors: a review,” *Nanotechnol. Rev.*, vol. 7, no. 1, pp. 19–41, 2018, https://doi.org/10.1515/ntrev-2017-0160.

[42] E. Asadian, M. Ghalkhani, and S. Shahrokhian, “Electrochemical sensing based on carbon nanoparticles: A review,” *Sensors Actuators B Chem.*, vol. 293, pp. 183–209, 2019, https://doi.org/10.1016/j.snb.2019.04.075.

[43] Annu, S. Sharma, R. Jain, and A. N. Raja, “Review—Pencil Graphite Electrode: An Emerging Sensing Material,” *J. Electrochem. Soc.*, vol. 167, no. 3, p. 037501, 2020, https://doi.org/10.1149/2.0012003JES.

[44] M. Sadl, U. Tomc, U. Prah, and H. Ursic, “Protective Alumina Coatings Prepared by Aerosol Deposition on Magnetocaloric Gadolinium Elements,” *Inf. MIDEM - J. Microelectron. Electron. Components Mater.*, vol. 49, no. 3, pp. 177–182, 2019, https://doi.org/10.33180/InfMIDEM2019.306.

[45] I. Stojanoska *et al.*, “Indium-zinc-oxide thin films produced by low-cost chemical solution deposition: Tuning the microstructure, optical and electrical properties with the processing conditions,” *Heliyon*, vol. 9, no. 9, p. e19744, 2023, https://doi.org/10.1016/j.heliyon.2023.e19744.

[46] I. Lavagnini, R. Antiochia, and F. Magno, “An Extended Method for the Practical Evaluation of the Standard Rate Constant from Cyclic Voltammetric Data,” *Electroanalysis*, vol. 16, no. 6, pp. 505–506, 2004, https://doi.org/10.1002/elan.200302851.

[47] D.-W. Lee *et al.*, “Experimental and numerical study for Cu metal coatings at room temperature via powder spray process,” *Surf. Coatings Technol.*, vol. 353, pp. 66–74, 2018, https://doi.org/10.1016/j.surfcoat.2018.08.075.

[48] S. S. Manokhin, V. Y. Barinov, and O. A. Golosova, “Aerosol Deposition of MAX Phase-Based Coatings onto High-Temperature Nickel Alloy,” *Int. J. Self-Propagating High-Temperature Synth.*, vol. 28, no. 3, pp. 210–212, 2019, https://doi.org/10.3103/S1061386219030087.

[49] S. Choi, J.-H. Lim, E.-Y. Kang, H. Kim, Y.-M. Kong, and D.-Y. Jeong, “Deposition behavior of glass thick film formation on substrates with different hardness by aerosol deposition,” *J. Asian Ceram. Soc.*, vol. 9, no. 3, pp. 1128–1136, 2021, https://doi.org/10.1080/21870764.2021.1943155.

[50] M. Hatala, P. Gemeiner, M. Hvojnik, and M. Mikula, “The effect of the ink composition on the performance of carbon-based conductive screen printing inks,” *J. Mater. Sci. Mater. Electron.*, vol. 30, no. 2, pp. 1034–1044, 2019, https://doi.org/10.1007/s10854-018-0372-7.

[51] “Int. Centre Diffraction Data (ICDD) PDF-4+/Web 2023.” 2023, https://www.icdd.com/assets/files/2023-PDF-4-Web-Flyer.pdf.

[52] J. Exner, M. Schubert, D. Hanft, J. Kita, and R. Moos, “How to treat powders for the room temperature aerosol deposition method to avoid porous, low strength ceramic films,” *J. Eur. Ceram. Soc.*, vol. 39, no. 2–3, pp. 592–600, 2019, https://doi.org/10.1016/j.jeurceramsoc.2018.08.008.

[53] M. Dekleva *et al.*, “An innovative pretreatment protocol to eliminate silver contamination-induced voltammetric interference on graphite-glass working electrode,” *Electrochem. commun.*, vol. 162, p. 107707, 2024, https://doi.org/10.1016/j.elecom.2024.107707.

[54] M. G. Trachioti, A. C. Lazanas, and M. I. Prodromidis, “Shedding light on the calculation of electrode electroactive area and heterogeneous electron transfer rate constants at graphite screen-printed electrodes,” *Microchim. Acta*, vol. 190, no. 7, p. 251, 2023, https://doi.org/10.1007/s00604-023-05832-w.

[55] A. Pop, I. Birsan, C. Orha, R. Pode, and F. Manea, “Carbon-Based Electrode for Parabens Detection,” vol. 10, no. 9, pp. 1228–1236, 2016, https://doi.org/10.5281/zenodo.1127017.

[56] P. K. Jiwanti, B. Y. Wardhana, L. G. Sutanto, and M. F. Chanif, “A Review on

Carbon-based Electrodes for Electrochemical Sensor of Quinolone Antibiotics," *ChemistrySelect*, vol. 7, no. 15, 2022, https://doi.org/10.1002/slct.202103997.

[57] W. Duan, M. R. Baez-Gaxiola, M. Gich, and C. Fernández-Sánchez, "Detection of chlorinated organic pollutants with an integrated screen-printed electrochemical sensor based on a carbon nanocomposite derived from bread waste," *Electrochim. Acta*, vol. 436, p. 141459, 2022, https://doi.org/10.1016/j.electacta.2022.141459.

[58] A. M. Abdel-Aziz, H. H. Hassan, and I. H. A. Badr, "Activated Glassy Carbon Electrode as an Electrochemical Sensing Platform for the Determination of 4-Nitrophenol and Dopamine in Real Samples," *ACS Omega*, vol. 7, no. 38, pp. 34127–34135, 2022, https://doi.org/10.1021/acsomega.2c03427.

Arrived: 19.04.2024

Accepted: 18.06.2024